IEEE Open Journal of the
Industrial Electronics Society

Received 28 November 2025; revised 19 January 2026; accepted 10 February 2026. Date of publication 13 February 2026;
date of current version 2 March 2026. The review of this article was arranged by Associate Editor H. Li.

Digital Object Identifier 10.1109/OJIES.2026.3664637

Integration of Battery Into Photovoltaic to Virtual Bus Parallel Differential Power Processing Architecture

AFSHIN NAZER [1], OLINDO ISABELLA [1], HANI VAHEDI [1], AND PATRIZIO MANGANIELLO [2]

[1]Delft University of Technology, 2628 CD Delft, The Netherlands
[2]Hasselt University, 3500 Hasselt, Belgium

CORRESPONDING AUTHOR: AFSHIN NAZER (e-mail: A.Nazer@tue.nl).

This work was supported by the Sector Plan of the Dutch Government in Photovoltatronics Research.

ABSTRACT This article introduces a parallel differential power processing (PDPP) architecture for photovoltaic (PV)/battery applications. The PV to Virtual Bus (PV2VB) architecture enables the integration of a battery and manages its power while performing maximum power point tracking on the PV strings. In the proposed PV2VB PDPP architecture, the battery is positioned at the virtual bus, acting as the input for all string-level converters (SLCs). By selecting a lower voltage for the battery at the virtual bus compared to the PV string or the main bus voltages, component voltage ratings can be reduced. The architecture employs dual active bridge converters connected to bridgeless (BL) converters as SLCs to generate both positive and negative output voltages while providing isolation. These SLCs track the maximum power point of each PV string, while the central converter manages battery charging and discharging. Experimental results confirm the performance and effectiveness of the proposed PV2VB PDPP architecture, achieving efficiencies between 95.5% and 99%.

INDEX TERMS Battery charger, differential power processing, partial shading, photovoltaic (PV) system, photovoltatronics.

I. INTRODUCTION

Over a century of dedicated research and development has resulted in high penetration of photovoltaic (PV) energy resources in the power system. A multitude of advantages underpins their widespread adoption, including abundance of free solar energy, eco-friendly operation, longevity (> 25 years), sustainable materials, simplicity in installation, minimal maintenance, and remote accessibility [1].

However, on one hand, PV systems have a high initial cost, so it is crucial to design and install PV with both high energy yield and low initial cost to enhance Levelized Cost of Energy (LCOE) [2], [3]. One innovative concept contributing to lowering LCOE is the DPP approach, which can be categorized as a facet of Distributed Maximum Power Point Tracking [4], [5], [6]. They are able to mitigate mismatch-related losses caused by factors such as partial shading, disparate PV module tilt angles, dust accumulation, and PV cell degradation. Moreover, they only process part of the power generated by the PV modules, while the remaining part (ideally, the majority) is directly delivered to the output. This brings two main advantages for DPPs: 1) improved cost and system's efficiency [7], [8], and 2) reduction of the stress on the components, which results in higher reliability and lifespan [9].

On the other hand, PV systems produce fluctuating and unreliable power due to their inherent intermittency. To address this issue, energy storage devices (ESDs) are commonly used alongside PV systems to stabilize output and enhance system reliability [10], [11]. As the penetration of PV systems increases, integrating them with ESDs becomes essential for grid connectivity. Amongst different technologies of ESDs, batteries are attracting much attention owing to advancements in battery technology, economies of scale in manufacturing, significant cost reductions, and efficiency improvements.

In a PV/battery architecture, along with two independent control variables, at least three power transmission branches exist: PV to load (PV-L), PV to battery (PV-B), and battery

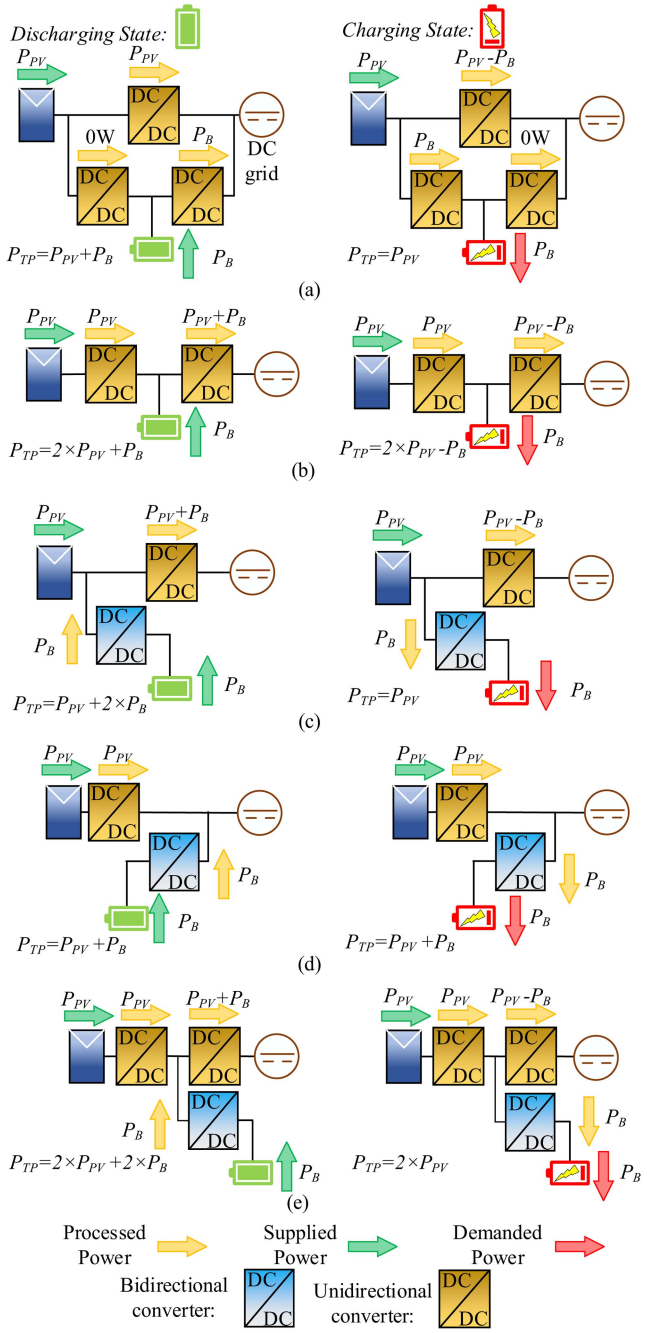

FIGURE 1. Four topological PV/battery architectures with indication of the power flow distribution. (a) 3U. (b) 2U. (c) 1U1B-I. (d) 1U1B-II. (e) 1B2U architectures. Ochre and blue DC–DC blocks represent unidirectional and bidirectional DC–DC converters, respectively.

to load (B-L). It is useful to note that the average power transmitted through the PV-L branch is typically significantly larger than that transmitted through the other two branches. Based on power transmission paths, PV/battery architectures can be typically categorized into four different architectures (see Fig. 1).

1) 3U, consisting of three unidirectional DC–DC converters [12], [13].
2) 2U, consisting of two unidirectional DC–DC converters [14], [15].
3) 1B1U, consisting of one bidirectional and one unidirectional DC–DC converter [16], [17], [18], [19].
4) 1B2U, consisting of one bidirectional and two unidirectional DC–DC converters [20], [21].

In the 3U architecture [see Fig. 1(a)], power transmission for each branch is achieved using a unidirectional two-port DC–DC converter, each with at least one independent control variable. Allocating one path for PV-L (high power) and another for PV-B/B-L (low power) allows the architecture to process less power overall (P_{TP}), resulting in high efficiency. However, the presence of three unidirectional DC–DC converters, and consequently three controllers, increases the system and control complexity and cost. To reduce complexity associated with the number of DC–DC converters, 2U architectures use the same path for all three power transmission branches [see Fig. 1(b)]. However, in this architecture, the power produced by the PV elements is processed twice to reach the load through the PV-L branch.

This deteriorates efficiency and increases converter's cost due to the requirement for two high-power DC–DC converters.

To address the issues of 2U architectures, 1B1U-I does not increase the processed power unlike in 2U architectures, since B-L power is lower than PV-L power transmission branches. Depending on the connection of the bidirectional DC–DC converter to either the PV or the load port, two different 1B1U architectures are possible: 1) 1B1U-I [16], [17] [see Fig. 1(c)] and 2) 1B1U-II [18] [see Fig. 1(d)]. Although the B-L power may be processed twice in 1B1U-I, it does not increase the processed power unlike in 2U architectures, since B-L power is lower than PV-L power, and there are still only two DC–DC converters as in 2U.

Considering both charging and discharging states, neither 1B1U-I nor 1B1U-II demonstrates a significant advantage over the other in terms of total processed power. 1B1U-I has a strong ability to adapt to variations in the output port, while in the 1B1U-II architectures, the PV port is well regulated with a dedicated bidirectional converter to adapt to changes in the output voltage/power of PV modules caused by different weather conditions. Unlike 1B1U-I, where the load is regulated solely by the unidirectional converter, 1B1U-II regulates the load voltage using either the unidirectional or bidirectional converter. This increases controller switching from one operation mode to another, leading to control complexity. Moreover, for AC grid connection, unlike 1B1U-II [22], 1B1U-I allows the integration of the unidirectional DC–DC converters' duties into the DC–AC inverters [16], improving cost and efficiency.

Eventually, the literature has reported on the 1B2U architectures [23] [see Fig. 1(e)]. This architecture suffers from several drawbacks. These include high architecture and control complexity, increased processing power, lower efficiency, and higher costs compared to other architectures.

TABLE 1. Comparison of PV/Battery Architectures

Feature \ Architecture	3U	2U	1U1B-I	1U1B-II	1B2U
Architecture complexity	Poor	Good	Ave	Ave	Poor
Cost	High	High	Ave	Ave	High
Control complexity	Poor	Good	Good	Poor	Poor
Efficiency (%)	High 91–96.2	Low 84.8–96.4	High 90.3–96.5	High 90.3–96.5	Low 88.7–94.3
Processed power	Low	High	Low	Low	High

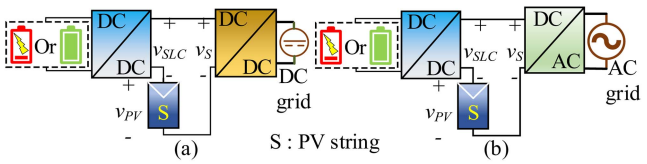

FIGURE 2. Proposed architectures for a single PV string connected to (a) DC and (b) AC grids. Ochre and blue DC–DC blocks represent unidirectional and bidirectional DC-DC converters, respectively.

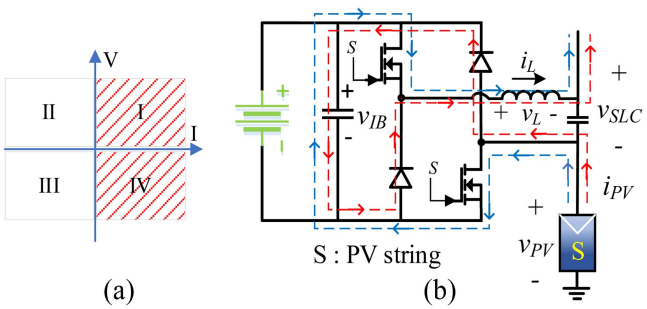

FIGURE 3. Bidirectional converter for the architecture of Fig. 2. (a) Required operational regions. (b) Implementation using a BL converter (Blue dashed-line: S is ON-state, Red dashed-line: S is OFF-state).

Based on the aforementioned analysis, the main characteristics of architectures are summarized in Table 1. It can be concluded that the 1B1U-I architecture generally offers the best overall performance. However, it still has three main downsides.

1) In applications where the PV voltage is higher than the battery voltage, the unidirectional converters in the 1B1U-I architecture must tolerate the high PV voltage. This requirement leads to increased losses and system costs.
2) If the PV part consists of PV strings and additional PV modules need to be added to a PV string, the converters must be replaced to handle the new PV string voltage. This necessity decreases the scalability of the architecture.
3) Last but not least, it is not feasible to extend the architecture to systems with multiple PV strings and independently track the maximum power point (MPP) of each PV string.

This article proposes a new system based on the PV to virtual bus parallel differential power processing (PV2VB PDPP) architecture. This architecture is closely aligned with the 1B1U-I architecture and retains all its advantages. Yet, it fully exploits the benefits of the PV2VB PDPP architecture to remove the weakness of 1B1U-I architectures, such as:

1) components requiring low blocking voltage in the bidirectional converter, leading to high efficiency and the advantages of low-voltage converters;
2) superior scalability and adaptability for integrating new PV modules to the PV strings [24], [25], [26], [27], which facilitates mass production and is expected to result in low production costs;
3) ability to perform string-level MPPT.

Besides, the lower component voltage ratings also help decrease repair expenses. By reducing stress on components and improving reliability and lifespan, the architecture ensures high availability and minimizes financial losses from downtime. Furthermore, its high efficiency reduces losses from power conversion, making it a cost-effective and versatile solution overall.

The remainder of this article is structured as follows: Section II introduces the proposed architecture for a single PV string, extends the architecture for multiple PV strings, and provides an in-depth analysis of the steady-state operation of both the central converter and SLCs, outlining their respective control objectives. Section III elaborates on all possible operational states of the architecture and provides a thorough analysis of the converters processed power and their losses. Section IV discusses the battery charging and discharging rate and the operational regions in which the architecture can function. Section V presents experimental results to validate the system's performance. Section VI concludes the article.

II. OPERATION OF THE PROPOSED PV2VB PDPP ARCHITECTURE

A. FOR A SINGLE PV STRING

In 1B1U-I architectures, the bidirectional converter operates in parallel with the PV string, adding or subtracting current to manage battery power injection or withdrawal. In contrast, the proposed architecture design utilizes a bidirectional converter that adds or subtracts surplus voltage to the PV string voltage to manage battery power injection or withdrawal (see Fig. 2). Consequently, this bidirectional converter must generate both positive and negative voltages, operating within the first and fourth quadrants of the V-I curve [see Fig. 3(a)], making a BL converter [see Fig. 3(b)] a suitable option.

In the BL converter, during the switche ON state, the voltage before the *LC* output filter (v_{IB}) polarity aligns with the intermediate bus voltage, discharging the capacitor. When the switches are OFF, the BL converter inverts the intermediate bus voltage, charging the capacitor. Predominantly maintaining the switches in the ON state during each switching period results in a positive voltage being added to the PV string, thus allowing average power flow from the battery to the string

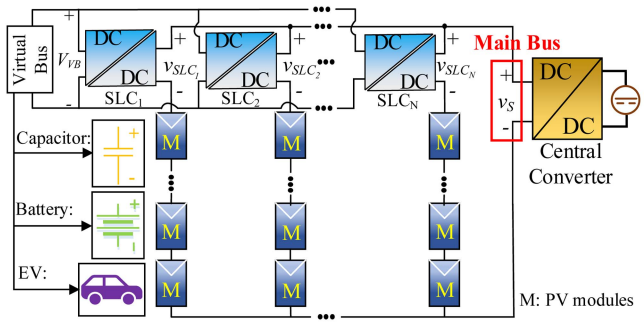

FIGURE 4. Proposed PV2VB PDPP architecture for multiple PV strings. Ochre and blue DC–DC blocks represent unidirectional and bidirectional DC–DC converters, respectively.

and vice versa. While the BL converter provides a straightforward and simple solution, it does not offer isolation between the battery and the PV strings. Depending on the topologies chosen for the bidirectional and unidirectional converters, the architecture can be designed to be nonisolated, partially isolated, or fully isolated.

Generally, two independent control variables are required for PV/battery architectures to perform battery charging and discharging with given profiles and MPPT. Traditionally, the bidirectional converter is used as an actuator to perform battery charging/discharging, while the unidirectional converter tracks the MPP of the PV string. However, in the proposed design, the bidirectional converter is used to perform MPPT, while the unidirectional converter controls the operation of the battery. The advantages will become clear in the next section when the proposed architecture with multiple PV strings is discussed.

B. FOR MULTIPLE PV STRINGS

To extend the proposed architectures for multiple PV strings, the storage ports can be paralleled as well as the grid ports, while each PV port is independently connected to a PV string. Then, it is possible to integrate all the unidirectional DC–DC converters, which are common among architectures, into a single central converter, as shown in Fig. 4. The final architecture, shown in Fig. 4, is called PV2VB PDPP architecture. With N_{PV} PV strings, this architecture has N_{PV} + 1 control objectives (N_{PV} PV strings and one battery), N_{PV} bidirectional converters (referred to as SLCs), and one unidirectional converter (referred to as the central converter), resulting in N_{PV} + 1 actuators. As mentioned previously, the SLCs primarily provide the required differential voltage between the PV strings and the main bus voltage to independently track each PV string's MPP. These SLCs are interconnected to a shared storage port, also known as the virtual bus, where the batteries are placed.

1) CENTRAL CONVERTER

The central converter controller is actuator to provide battery profile control, which is done by regulating the main bus voltage. If the assumption of lossless converters is considered for the sake of simplicity, the following relationship can be derived for the proposed architecture:

$$p_{\text{out}} = p_{\text{in}} + p_B. \tag{1}$$

In the context of the PV2VB PDPP architecture, p_B, p_{out}, and p_{in} represent the battery power, the power delivered to the main bus, and the power generated by the PV strings, respectively. These powers can be computed as follows:

$$p_{\text{out}} = v_S \times i_S = v_s \times \sum_{i=1}^{N_{\text{PV}}} i_{\text{PV}_i} \tag{2}$$

$$p_{\text{in}} = \sum_{i=1}^{N} v_{\text{PV}_i} \times i_{\text{PV}_i} \tag{3}$$

where v_s, i_s, v_{PV_i}, and i_{PV_i} are the main bus voltage, the main bus current, the ith PV string's voltage, and the ith PV string's current, respectively. The following steady-state equation can be obtained by substituting (2) and (3) in (1)

$$P_B = V_S \times \sum_{i=1}^{N_{\text{PV}}} I_{\text{PV}_i} - \sum_{i=1}^{N_{\text{PV}}} V_{\text{PV}_i} \times I_{\text{PV}_i}. \tag{4}$$

Note that, in (4) and in the rest of the manuscript, capital letters indicate the steady-state value of the variables. Since it is desirable for the PV strings to operate at their MPP in order to maximize system efficiency and the main bus current equals the summation of PV strings' current, the main bus voltage (V_S) serves as the sole actuator to control charging and discharging of the battery. An increase in the main bus voltage signifies greater energy demand, resulting in either reduced charging rate of the battery or increasing discharging rate of the battery.

The output voltage of the ith SLC can be expressed as

$$V_{\text{SLC}_i} = V_S - V_{\text{PV}_i}. \tag{5}$$

By substituting (5) in (4), we have

$$P_B = \sum_{i=1}^{N_{\text{PV}}} V_{\text{SLC}_i} \times I_{\text{PV}_i} \tag{6}$$

given that I_{PV_i} is consistently positive, (6) shows that SLCs must generate negative and positive output voltage to charge and discharge the battery. To clarify further, if the ith SLC generates a negative output voltage, the associated PV string assists in charging the battery, and conversely, when the output voltage is positive, the string discharges the battery.

The block diagram in Fig. 5 illustrates the PV2VB PDPP architecture alongside its control structures. A desired algorithm sets the battery's current/voltage reference, which is compared to actual values. Errors are sent to the central controller, which adjusts the main bus voltage via the central converter to achieve the desired battery parameters. Various charging/discharging methods, including constant current, constant voltage, and multistage charging [28], [29], can be applied to the PV2VB PDPP architecture.

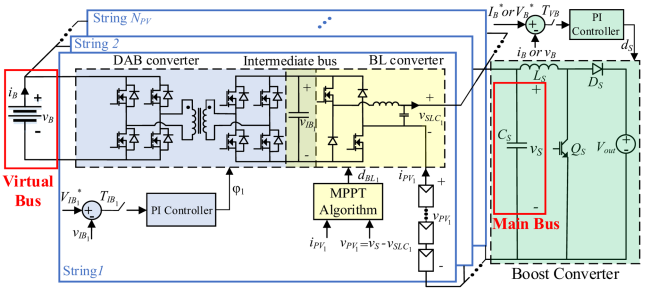

FIGURE 5. PV2VB PDPP architecture with its control loop block diagrams for PV/Battery system (∗: indicates reference value).

TABLE 2. Operation Modes of PV/Battery Architectures

Mode		Input	Output	Proposed System ability
SIDO	I	PV	Battery & Grid	Yes
DISO	I	PV & Battery	Grid	Yes
	II	PV & Grid	Battery	No
SISO	I	PV	Battery	Limited[1]
	II	PV	Grid	Yes
	III	Grid	Battery	Yes[2&3]
	IV	Battery	Grid	Yes[3]

1: In this mode, the PV strings may not work at their MPP.
2: If the central converter is bidirectional.
3: By bypassing the PV strings and reconfiguring the architecture (Figure 8)

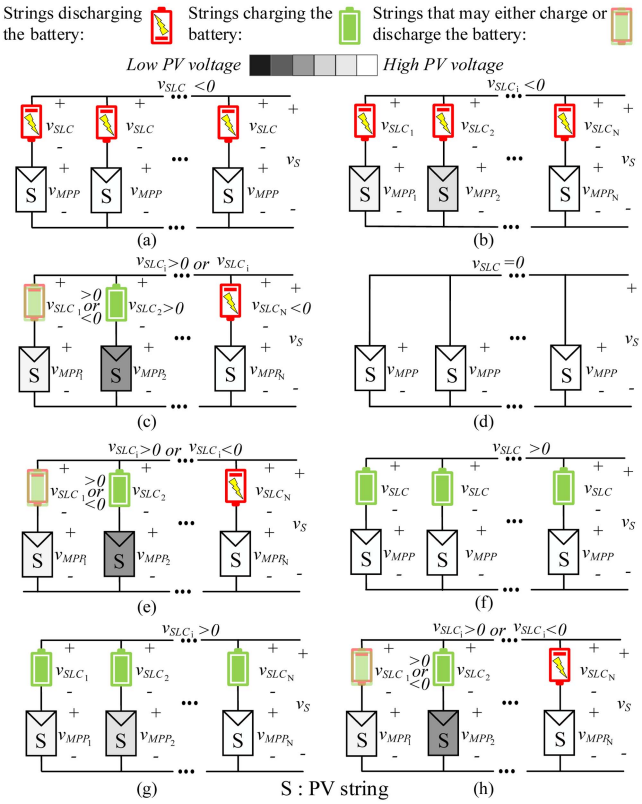

FIGURE 6. Simplified PV2VB PDPP architecture when the architecture is in state (a) 1, (b) 2, (c) 3, (d) 4, (e) 5, (f) 6, (g) 7, and (h) 8.

2) STRING-LEVEL CONVERTERS

When the architecture is extended for multiple PV strings, the SLCs must include an additional feature: isolation. This isolation is essential to prevent the current from the PV strings from circulating through incorrect paths. Therefore, in the proposed SLC topology, illustrated in Fig. 5, two stages are employed: a DAB converter followed by a BL converter, with capacitors forming an intermediate bus to decouple their performance. BL converters are responsible for tracking MPP of voltage (v_{IB}), DAB converters with single phase shift modulation [30] are utilized, facilitating power transfer between the virtual bus and the intermediate bus, which are the primary and secondary sides, respectively. Thus, the DAB converter must effectively regulate these intermediate bus voltages to ensure stable and efficient operation [24]. The architecture has at least partial isolation within the system, between the battery and PV elements. This isolation is crucial for onboard battery chargers to ensure double-fault protection and enhance user safety in plug-in hybrid electric vehicles [31].

III. PROPOSED ARCHITECTURE STATES, PROCESSED POWER, AND LOSS ANALYSIS

A. STATES

Generally, when the system directs power from one port to the other two, the architecture operates in single-input dual-output (SIDO) mode. In dual-input single-output (DISO) mode, power flows from two ports to the remaining one. When a port does not participate, the architecture is in single-input single-output (SISO) mode. Table 2 shows the operation modes and port statuses.

The proposed architecture does not allow for the simultaneous operation of PV and grid as input, making the DISO-II mode outlined in Table 2 unfeasible within this framework. In SISO-I mode, the central converter is bypassed, allowing the PV string to connect directly to the input of the SLCs and charge the battery. Since the maximum voltage of the SLCs is lower than the nominal MPP voltage of the PV string, the PV string will not operate at its MPP. However, this limitation is not necessarily a disadvantage, as in other architectures, where in this mode the power output is constrained by the battery's demand, which may also prevent the PV strings, to ensure stability of the intermediate bus, the PV strings are prevented from operating at their MPP. To enable SISO-IV mode, the PV string must be bypassed (see Fig. 10), allowing the battery to supply power directly to the grid.

If the central converter is bidirectional, it is possible to operate in SISO-III mode through this architecture; however, this aspect falls outside the scope of this article. Therefore, this section mainly focuses on the architecture operation in SIDO-I, DISO-I, and SISO-II modes. These subset of operation modes results in the architecture possibly operating in eight distinct states, outlined in Table 3.

TABLE 3. States of PV2VB PDPP Architecture Based on Battery Status and Mismatches Among PV String MPP Voltages

Battery status	Charging			Resting		Discharging		
MPP voltage Mismatches	No	Yes		No	Yes	No	Yes	
SLCs Voltage	Negative	Negative	Both	0*	Both	Positive	Positive	Both
State	1	2	3	4	5	6	7	8
Operation Mode	SIDO-I			SISO-II		DISO-I		

* In practice, the SLCs operate with a slightly negative voltage to compensate for their losses.

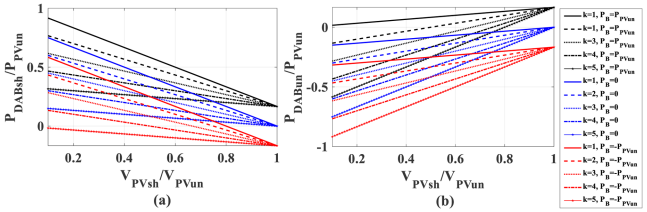

FIGURE 7. Influence of voltage difference among PV strings on processed power of DAB converters (a) connected to the shaded PV strings, and (b) connected to the unshaded PV strings ($N_{PV} = 6$, $\frac{I_{PV_{sh}}}{I_{PV_{un}}} = 1$).

Generally, the power delivered to the virtual bus from the ith PV string (P_{PV_i2VB}) and the battery charging rate (P_B)are given by

$$P_{PV_i2VB} = \left(V_S - V_{PV_i}\right) \times I_{PV_i} \tag{7}$$

$$P_B = \sum_{i=1}^{N_{PV}} \left(\left(V_S - V_{PV_i}\right) \times I_{PV_i}\right). \tag{8}$$

1) STATE 1

No MPP voltage mismatch, battery charging [see Fig. 6(a)]: Central controller lowers the main bus voltage below PV string voltages, producing negative SLC voltages. Power flows from the PV strings to the battery, with each string's contribution proportional to its MPP current

$$P_{PV_i2VB} = (V_S - V_{MPP}) \times I_{MPP_i}, V_S < V_{MPP} \tag{9}$$

$$P_B = (V_S - V_{MPP}) \sum_{i=1}^{N_{PV}} I_{MPP_i}, V_S < V_{MPP} \tag{10}$$

where I_{MPP_i} represents the MPP current of the ith PV string and V_{MPP} is the MPP voltage of all PV strings. In this state, the contribution of each PV string to the power supplied to the battery is directly proportional to its current.

2) STATE 2

Small MPP voltage mismatch, battery charging [see Fig. 6(b)]: Each PV string's contribution depends on both its current and voltage. Higher voltage strings generate larger negative SLC voltages, contributing more power to the battery

$$P_{PV_i2VB} = \left(V_S - V_{MPP_i}\right) \times I_{MPP_i}, V_S < V_{MPP_i} \tag{11}$$

$$P_B = \sum_{i=1}^{N_{PV}} \left(\left(V_S - V_{MPP_i}\right) \times I_{MPP_i}\right), V_S < V_{MPP_i} \tag{12}$$

where V_{MPP_i} represents the MPP voltage of the ith PV string.

3) STATE 3

Large MPP voltage mismatch, battery charging [see Fig. 6(c)]: Some PV strings' voltages drop, so they draw power from the virtual bus to operate at MPP, while others still transfer power to the battery. Overall, the battery is still charged. Equations are same as (7) and (8).

4) STATE 4

No MPP voltage mismatch, battery resting [see Fig. 6(d)]: SLCs ideally generate zero voltage or low negative voltage to compensate for converter losses. Central converter tracks MPP of all PV strings

$$P_{PV_i2VB} = P_B = 0, V_S \cong V_{MPP}. \tag{13}$$

5) STATE 5

MPP voltage mismatch, battery resting [see Fig. 6(e)]: PV strings with higher MPP voltages inject energy, while strings with lower MPP voltage draw energy via the virtual bus. Battery is idle; parallel capacitors, typically situated in that position for power smoothing and stabilization, handle energy exchange. Main bus voltage is the weighted average of PV voltages

$$P_{PV_i2VB} = \left(V_S - V_{MPP_i}\right) \times I_{MPP_i}, P_B = 0 \tag{14}$$

$$V_S = \frac{\sum_{i=1}^{N_{PV}} V_{MPP_i} \times I_{MPP_i}}{\sum_{i=1}^{N_{PV}} I_{MPP_i}}. \tag{15}$$

6) STATE 6

No MPP voltage mismatch, battery discharging [see Fig. 6(f)]: Main bus voltage is higher than PV voltages, producing positive SLC voltages. Power flows from the battery to PV strings

$$P_{PV_i2VB} = (V_S - V_{MPP}) \times I_{MPP_i}, V_S > V_{MPP} \tag{16}$$

$$P_B = (V_S - V_{MPP}) \sum_{i=1}^{N_{PV}} I_{MPP_i}, V_S > V_{MPP}. \tag{17}$$

7) STATE 7

Small MPP voltage mismatch, battery discharging [see Fig. 6(g)]: Strings with lower MPP voltage produce higher

positive SLC voltages, contributing more to discharge. Power contribution depends on both voltage and current

$$P_{\mathrm{PV}_i\mathrm{2VB}} = \left(V_S - V_{\mathrm{MPP}_i}\right) \times I_{\mathrm{MPP}_i}, V_S > V_{\mathrm{MPP}_i} \tag{18}$$

$$P_B = \sum_{i=1}^{N_{\mathrm{PV}}} \left(\left(V_S - V_{\mathrm{MPP}_i}\right) \times I_{\mathrm{MPP}_i}\right), V_S > V_{\mathrm{MPP}_i}. \tag{19}$$

8) STATE 8

Large MPP voltage mismatch, battery discharging [see Fig. 6(h)]: Some PV strings inject energy to the virtual bus while others draw energy. Battery still provides net power to the system. Equations are the same as (7) and (8).

B. PROCESSED POWER ANALYSIS

A complete analysis of processed power was conducted in [24] for the PV2VB PDPP for a purely capacitive virtual bus, which represents only the resting state of the architecture proposed in this article. To extend the analysis to charging and discharging statuses, (16) in [24] must be modified as follows:

$$P_{\mathrm{DAB}_j} = \left(\frac{P_B + \sum_{j=1}^{N_{\mathrm{PV}}} V_{\mathrm{PV}_j} \times I_{\mathrm{PV}_j}}{\sum_{j=1}^{N_{\mathrm{PV}}} I_{\mathrm{PV}_j}} - V_{\mathrm{PV}_j}\right) \times I_{\mathrm{PV}_j}. \tag{20}$$

Similarly to the analysis in [24], in a PV system consisting of N_{PV} PV strings, let k of these PV strings be shaded, producing voltage and currents of

$$I_{\mathrm{PV}_j}\big|_{j=1,2,..,k} = I_{\mathrm{PV_{sh}}} \quad V_{\mathrm{PV}_j}\big|_{j=1,2,..,k} = V_{\mathrm{PV_{sh}}}. \tag{21}$$

The remaining unshaded strings generate a current and a voltage of

$$I_{\mathrm{PV}_j}\big|_{j=k+1,...,N_{\mathrm{PV}}} = I_{\mathrm{PV_{un}}} \quad V_{\mathrm{PV}_j}\big|_{j=k+1,...,N_{\mathrm{PV}}} = V_{\mathrm{PV_{un}}}. \tag{22}$$

Considering (20)–(22), the power processed by DAB converters connected to the shaded and unshaded PV strings is determined as

$$P_{\mathrm{DAB_{sh}}} = \frac{P_B + (N_{\mathrm{PV}} - k) \times I_{\mathrm{PV_{un}}} \times \left(V_{\mathrm{PV_{un}}} - V_{\mathrm{PV_{sh}}}\right)}{\left((N_{\mathrm{PV}} - k) \times I_{\mathrm{PV_{un}}} + k \times I_{\mathrm{PV_{sh}}}\right)} \times I_{\mathrm{PV_{sh}}} \tag{23}$$

$$P_{\mathrm{DAB_{un}}} = \frac{P_B + k \times I_{\mathrm{PV_{sh}}} \times \left(V_{\mathrm{PV_{sh}}} - V_{\mathrm{PV_{un}}}\right)}{\left((N_{\mathrm{PV}} - k) \times I_{\mathrm{PV_{un}}} + k \times I_{\mathrm{PV_{sh}}}\right)} \times I_{\mathrm{PV_{un}}}. \tag{24}$$

Figs. 7(a) and 8(a), generated using (23), show the effect of voltage and current variations among PV strings on the processed power of DAB converters connected to shaded PV strings under different battery conditions. Similarly, Figs. 7(b) and 8(b), based on (24), illustrate the corresponding effect on the processed power of DAB converters connected to unshaded PV strings. It should be noted that in these figures, the sign of the normalized power indicates the direction of power flow: a positive value corresponds to power transfer from the battery to the PV string, while a negative value indicates power transfer from the PV string to the battery.

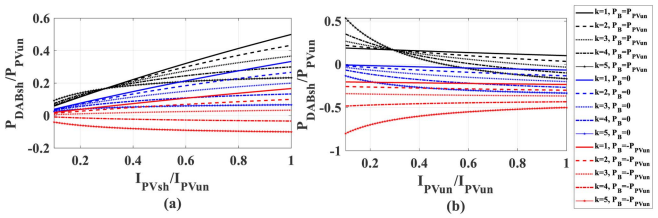

FIGURE 8. Influence of current difference among PV strings on processed power of DAB converters (a) connected to the shaded PV strings (b) connected to the unshaded PV strings ($N_{\mathrm{PV}} = 6$, $\frac{V_{\mathrm{PV_{sh}}}}{V_{\mathrm{PV_{un}}}} = 0.6$).

In Fig. 7, when the battery power is zero (resting, blue curves), the analysis of processed power by the DAB converters matches the results discussed in [24]. When the battery is charging (red curves, $P_B < 0$) and no shading is present ($\frac{V_{\mathrm{PV_{sh}}}}{V_{\mathrm{PV_{un}}}} = 1$), all DAB converters equally process power toward the battery (State 1). As the voltage difference between shaded and unshaded PV strings increases ($\frac{V_{\mathrm{PV_{sh}}}}{V_{\mathrm{PV_{un}}}} \to 0$), the unshaded converters process more power than the shaded ones (State 2). Eventually, the DAB converters connected to shaded strings begin transferring power from the battery to the PV strings, marking the transition to State 3. Similarly, when the battery is discharging (black curves, $P_B > 0$) and no shading is present, all DAB converters equally process power toward the strings (State 6). As the voltage difference grows, the DAB converters connected to shaded PV strings process more power than the unshaded ones (State 7). At some point, the DAB converters connected to the unshaded strings begin transferring power from the PV strings to the battery, which corresponds to State 8.

Fig. 8 shows that when the battery is either charging or discharging, the magnitude of the DAB processed power increases (i.e., more curves shift toward negative or positive values) compared to when the battery is resting. Another important trend to observe is that as the current of a shaded PV string increases, its processed power also increases. This is because, as expressed by (23) and (24), the processed power of each DAB is directly dependent on the current of its corresponding PV string. The explanation for the behavior of the individual curves is similar to [24]. Thus, the DAB converters may only need to be rated for a fraction of the PV string's peak power, which allows for reductions in both converter size and overall system cost. It should be noted that as the battery's nominal power increases, the rating of DAB converters will also need to increase.

BL converters differ from DAB converters in their rating approach, which is relatively simple to determine. Since BL converters must always conduct the current from their associated PV string, their current rating is directly defined by the current of such string. The voltage rating, however, depends on the chosen intermediate bus voltage. Because this bus voltage can be set lower than the PV string voltage, the component ratings of a BL converter can be reduced compared to the PV

string rating. Note that the PV string rating determines the power rating of the SLCs in a full power processing (FPP) architecture.

C. LOSS ANALYSIS

The DAB converter contains an isolated transformer and a larger number of switches compared to the BL converter; therefore, it would incur higher losses if both would process the same amount of power. However, as shown in the previous section, the DAB converter processes less power than the BL converter, (and the BL stage still processes less power compared to an FPP architecture [24]).

Specifically, the power $P_{\mathrm{PV}_i\mathrm{2VB}}$ is processed by the DAB converter. Accordingly, the DAB losses ($P_{\mathrm{loss}_{\mathrm{DAB}_i}}$) can be expressed as

$$P_{\mathrm{loss}_{\mathrm{DAB}_i}} = (1-\eta_{\mathrm{DAB}})\ P_{\mathrm{PV}_i\mathrm{2VB}} \tag{25}$$

where η_{DAB} is the efficiency of the DAB converters.

On the other hand, the power processed by the BL stage is defined by the current from its associated PV string and the intermediate bus voltage. Therefore, the BL losses ($P_{\mathrm{loss}_{\mathrm{BL}_i}}$) are given by

$$P_{\mathrm{loss}_{\mathrm{BL}_i}} = (1-\eta_{\mathrm{BL}})\ V_{\mathrm{IB}_i} \times I_{\mathrm{MPP}_i} \tag{26}$$

where η_{BL} is the efficiency of the BL converters. Therefore, the SLCs' power losses ($P_{\mathrm{loss}_{\mathrm{SLC}_i}}$) can be calculated as

$$P_{\mathrm{loss}_{\mathrm{SLC}_i}} = (1-\eta_{\mathrm{DAB}})\,P_{\mathrm{PV}_i\mathrm{2VB}} + (1-\eta_{\mathrm{BL}})\,V_{\mathrm{IB}_i} \times I_{\mathrm{MPP}_i}. \tag{27}$$

IV. RATE OF THE BATTERY CHARGE AND DISCHARGE

In Section III, different states in which the architecture can operate are presented, being imposed by weather conditions and the battery charging/discharging statutes. However, if the SLCs voltage ratings are not designed properly, the architecture can be unable to fulfill the expected duties. Therefore, an analysis similar to [24], where the virtual bus consists solely of capacitors, is required to properly design the PV/battery system.

Let $V_{\mathrm{PV}_{\mathrm{MPP}_{\mathrm{min}}}}$ and $V_{\mathrm{PV}_{\mathrm{MPP}_{\mathrm{max}}}}$ be the minimum and maximum MPP voltage of PV strings, respectively. If the SLC's maximum voltage ($\pm V_{\mathrm{SLC}_{\mathrm{max}}}$)is selected properly, five regions emerge, separated by points A, B, D, and E (see Fig. 9) [24]

$$A = \left(V_{\mathrm{PV}_{\mathrm{MPP}_{\mathrm{min}}}} - V_{\mathrm{SLC}_{\mathrm{max}}}\right),\ B = \left(V_{\mathrm{PV}_{\mathrm{MPP}_{\mathrm{max}}}} - V_{\mathrm{SLC}_{\mathrm{max}}}\right) \tag{28}$$

$$D = \left(V_{\mathrm{PV}_{\mathrm{MPP}_{\mathrm{min}}}} + V_{\mathrm{SLC}_{\mathrm{max}}}\right), E = \left(V_{\mathrm{PV}_{\mathrm{OC}_{\mathrm{max}}}} + V_{\mathrm{SLC}_{\mathrm{max}}}\right).$$

In the first two regions, a low v_{s} causes all or some SLCs to operate at their maximum inverted voltage ($-V_{\mathrm{SLC}_{\mathrm{max}}}$). Consequently, none of the PV strings operate at their MPP (no MPPT region), or a subset (N_1) operates at their MPP while the remaining N_2 PV strings do not (pre-complete MPP region). In these regions, the battery is being continuously charged

$$P_B = \sum_{i=1}^{N_{\mathrm{PV}}} V_{\mathrm{SLC}_{\mathrm{max}}} \times I_{\mathrm{MPP}_i},\ 0 \le v_{\mathrm{s}} < A \tag{29}$$

$$P_B = \sum_{i=1}^{N_1} \left(V_{\mathrm{MPP}_i} - v_{\mathrm{s}}\right) I_{\mathrm{MPP}_i} + V_{\mathrm{SLC}_{\mathrm{max}}} \sum_{i=1}^{N_2} I_{\mathrm{SC}_i},\ A \le v_{\mathrm{s}} < B. \tag{30}$$

On the other hand, in the last two regions (beyond point D), v_{s} is so high that some PV strings no longer operate at their MPP. In essence, within the post-complete MPP region, N_3 PV strings reach the open circuit voltage, N_4 PV strings operate at ($v_s - V_{\mathrm{SLC}_{\mathrm{max}}}$), which is between their open circuit voltage and their MPP voltage, and N_5 PV strings operate at their MPP. In these regions, the battery is being discharged

$$P_B = -V_{\mathrm{SLC}_{\mathrm{max}}} \sum_{i=1}^{N_4} I_{\mathrm{PV}_i} + \sum_{i=1}^{N_5} \left(V_{\mathrm{MPP}_i} - v_{\mathrm{s}}\right) I_{\mathrm{MPP}_i},\ D \le v_{\mathrm{s}} < E. \tag{31}$$

At point E, all PV strings reach their open-circuit voltage, resulting in no power production.

Between points B and D is the desired operating region, called "Complete MPPT," where all PV strings work at MPP

$$P_B = \sum_{i=1}^{N_{\mathrm{PV}}} \left(V_{\mathrm{MPP}_i} - v_{\mathrm{s}}\right) I_{\mathrm{MPP}_i},\ B \le v_{\mathrm{s}} < D. \tag{32}$$

To ensure the existence of this region, it is imperative for point D to be positioned to the right of point B, which means

$$V_{\mathrm{SLC}_{\mathrm{max}}} \ge \frac{V_{\mathrm{PV}_{\mathrm{MPP}_{\mathrm{max}}}} - V_{\mathrm{PV}_{\mathrm{MPP}_{\mathrm{min}}}}}{2}. \tag{33}$$

In the complete MPPT region, the architecture can effectively track the PV string MPP and manage battery charging/discharging rates as per (4). A specific range for the rate of battery charging/discharging is depicted in Fig. 9.

When mismatches are minimal, where $V_{\mathrm{PV}_{\mathrm{MPP}_{\mathrm{max}}}}$ is close or equal to $V_{\mathrm{PV}_{\mathrm{MPP}_{\mathrm{min}}}}$, the absolute maximum rate of battery

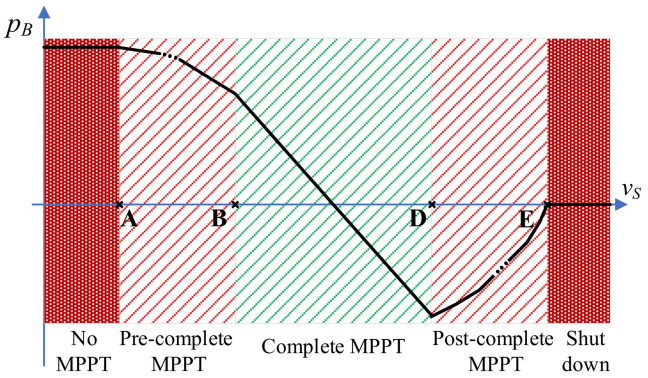

FIGURE 9. Rate of the battery charging/discharging.

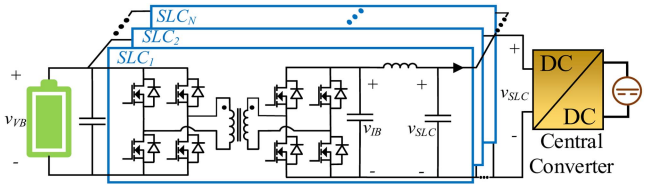

FIGURE 10. Reconfigured PDPP architecture during low sun irradiance and battery discharging, such as at night.

TABLE 4. Prototype Electrical Specifications and Component Parameters

	Parameter	Symbol	Value
Electrical specifications	PV/Battery rated power	P_{sys}	4.6 kW
	Battery voltage	V_{VB}	200 V
	MPP voltage at STC	V_{MPP}	390 V
	MPP current at STC	I_{MPP}	5.3 A
	SLC rated current	I_{SLC}	5 A
	SLC rated voltage	V_{SLC}	200 V
	Number of PV strings	N_{PV}	2
	Switching frequency	f_{sw}	100 kHz
Components parameters	Virtual bus capacitance	C_{VB}	1.2 mF
	BL inductance	L_{BL}	660 μH
	BL capacitor	C_{BL}	3 μF
	DAB leakage inductor	L_{DAB_L}	22 μH
	Boost inductor	L_S	510 μH
	Bus capacitor	C_S	6.6 μF

charging/discharging can be achieved by

$$P_B = \pm \sum_{i=1}^{N_{\text{PV}}} V_{\text{SLC}_{\max}} \times I_{\text{MPP}_i}. \tag{34}$$

Based on (33) and (34), increasing $V_{\text{SLC}_{\max}}$ allows for a greater MPPT range, enhancing the system's capability to handle more severe mismatch conditions, and increasing the absolute maximum rate of battery charging/discharging.

Equation (34) reveals that the rate of battery charging or discharging is contingent upon the PV string currents. In SISO-IV, the PV string current does not flow, so utilizing the battery to supply the grid or vice versa becomes unfeasible. To address the issue, bypassing the PV strings with diodes and activating the switches of the BL converters can reconfigure the system, as depicted in Fig. 10, enabling SISO-III and SISO-IV modes.

V. EXPERIMENTAL RESULTS

This section highlights the proposed architecture's ability to perform MPPT at the string level while regulating battery charge and discharge rates, demonstrating the feasibility of battery integration into the PV2VB PDPP system and exploring its operational states under varying conditions. Table 4 summarizes the prototype's electrical specifications and component values. As shown in Fig. 11, the experiments were conducted indoors using one 6210H-600S programmable DC supply to emulate a PV string and three SM1500-CP-30 bi-directional DC power supplies as the second PV string, battery emulator, and DC output of the central converter (V_{out} in Fig. 5). Both the intermediate bus voltage and the virtual bus (battery) voltage were set to 200 V, enabling a 1:1 DAB converter with symmetrical implementation and low-voltage devices on both sides. Nonetheless, these voltages can also be selected independently.

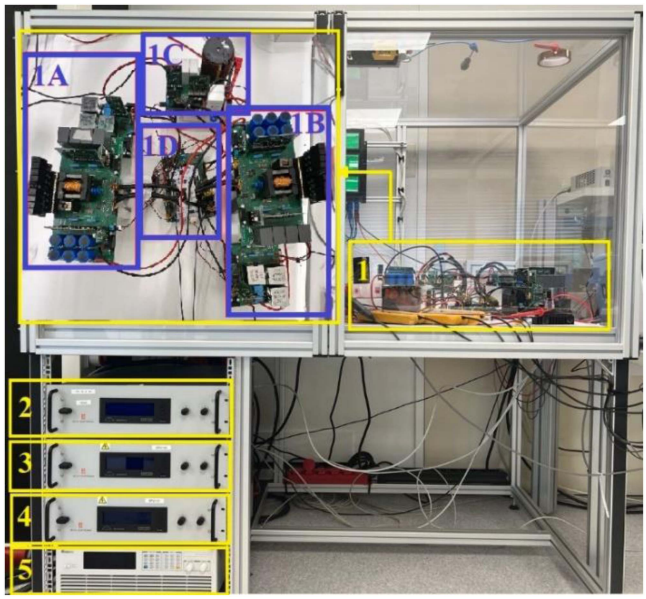

FIGURE 11. Photograph of the PV2VB PDPP architecture prototype. 1 A: SLC1, 1 B: SLC2, 1 C: Central converter, 1 D: Micro controller. 2, 3, and 4: SM1500-CP-30 Bi-directional DC power supplies, 5: 6210H-600S programmable DC power supply.

TABLE 5. Experimental Operation Points for the Architecture

	Battery Charge rate	PV string 1 MPP point	PV string 2 MPP point	Main bus voltage*
State 1	-480 W	380 V/5.3 A	380 V/ 5.3 A	334
State 2	-480 W	350 V/5.3 A	380 V/ 5.3 A	320
State 3	-240 W	270 V/ 5.3 A	380 V/ 5.3 A	302
State 4	0 W	380 V/ 5.3 A	380 V/ 5.3 A	380
State 5	0 W	350 V/ 5.3 A	380 V/ 5.3 A	365
State 6	480 W	380 V/ 5.3 A	380 V/ 5.3 A	425
State 7	480 W	350 V/ 5.3 A	380 V/ 5.3 A	410
State 8	240 W	290 V/ 5.3 A	380 V/ 5.3 A	357

* Expected main bus voltage based on (4).

A. STRING LEVEL MPPT AND BATTERY CHARGING/DISCHARGING

The operation of the proposed two-string PV architecture was validated experimentally using a Perturb and Observe algorithm with a 20 ms perturbation period and 5% duty cycle step size. Under standard test conditions, each PV string produces 390 V and 5.3 A. A boost converter was selected as the central converter to manage battery energy through a PI controller with an 80 ms sampling time. As summarized in Table 5, various battery charge/discharge states and PV string mismatches were tested to cover all operating conditions. The virtual bus, emulated as a 200 V battery stack, defines the SLC voltage rating.

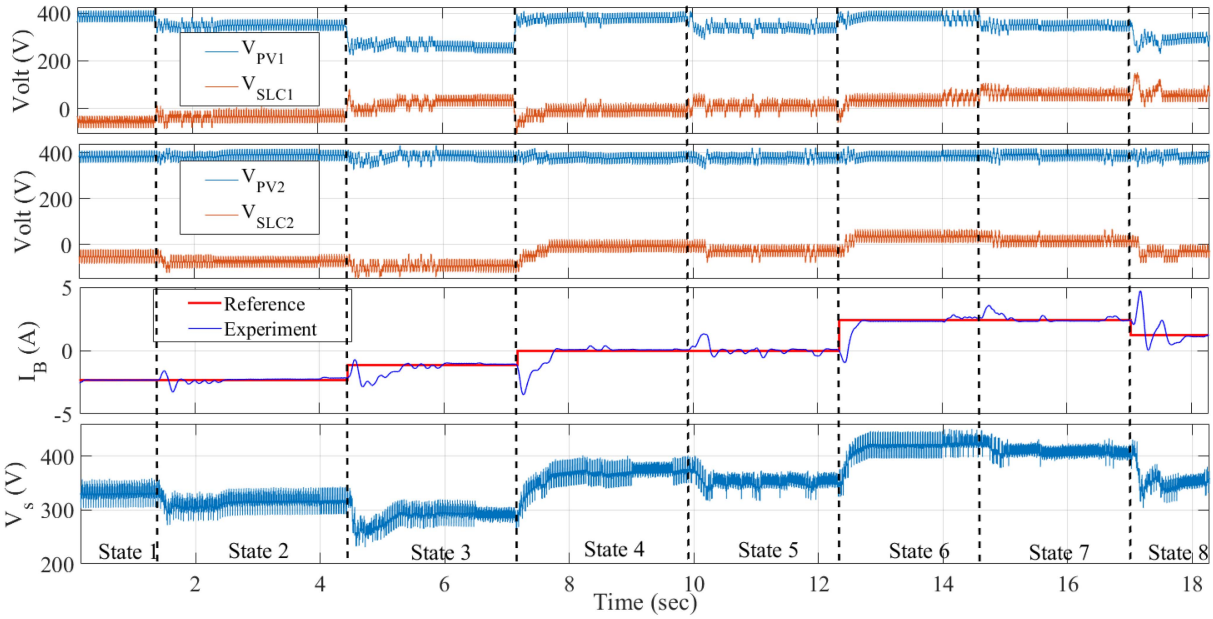

FIGURE 12. Experimental results of the PDPP architecture in different operation states based on operation points shown in Table 5.

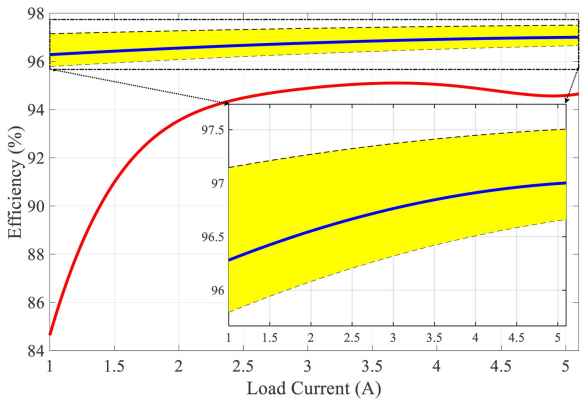

FIGURE 13. Averaged system efficiency (Blue line) and a single SLC efficiency (Red line) as a function of load current.

Initially, PV strings operate under uniform conditions, and the battery is charged at a rate of 480 W. Therefore, the system is in state 1, as shown in Fig. 12 , with the main bus voltage below both PV string voltages. It results in both SLCs generating negative voltages, meaning that both PV strings contribute to charging the battery. After around 1.3 s, a small mismatch is introduced between the PV strings while the battery continues to charge at 480 W. This transition moves the system to state 2, where the main bus voltage remains below both PV string voltages. As a result, SLCs still generate negative voltages, and PV strings continue to charge the battery. At 4.4 s, a significant mismatch is applied between the PV strings, and the battery is charging at 240 W, moving the system into state 3. Therefore, the main bus voltage is lower than the PV string 2 voltage but higher than PV string 1 voltage. This means PV string 1(shaded PV string) no longer contributes to injecting energy into the virtual bus and instead draws energy from it to operate at its MPP.

At 7.2 s, the battery is resting with no mismatches and minor mismatches between PV strings voltage applied at 9.9 s. As shown in Fig. 12, the SLCs generate a voltage close to zero when there are no mismatches. Although it is expected that SLCs generate absolute zero voltage based on (4), small negative voltage has been generated because of the converter's losses. When mismatches occur, some SLCs generate positive voltage while others generate negative voltage, leading to zero average power on the virtual bus, allowing the battery to rest.

In the next approximately 4 s, the battery starts discharging, directing power to the output. When there are no mismatches or minor mismatches among the PV string voltages, the SLCs generate a positive voltage. Since the current output of SLCs is positive, the battery power can pass to the output. However, at the 17 s, a significant mismatch among PV string voltages occurs. Therefore, the SLC corresponding to PV string 2 (unshaded PV string), which has the higher voltage, generates negative voltage, resulting in PV string 2 sending power to the virtual bus to maintain its MPP.

Ultimately, experiments verify that the architecture is capable of setting an appropriate main bus voltage to charge, discharge, or rest the battery, facilitating effective energy management while tracking the MPP of PV strings.

B. PV2VB PDPP ARCHITECTURE EFFICIENCY

This section analyzes the conversion efficiency of the proposed architecture, excluding the MPPT efficiency (i.e., assuming no oscillation around the MPP). For the efficiency analysis, the power delivered to the main bus is considered as the power output. The input power corresponds to the power generated by the PV strings, while the battery power is treated as either an input or an output, depending on whether the battery is charging or discharging. The efficiency of the SLCs was measured under the following conditions: 200 V input

(virtual bus) voltage, load voltage between −55 and 55 V, and varying load current between 1 and 5 A. It shows that under these conditions, the average efficiency of a single SLC ranges from 84.4% to 95.1%.

Similarly, the efficiency of the PV2VB PDPP architecture with an integrated battery was measured with the SLCs under the same conditions. PV string 2 was kept constant at 380 V and 5.3 A, while the battery current was adjusted from −3 A to 3 A, and PV string 1 current (called a load current) from 1 to 5 A. Efficiency was measured at over 130 different operating points. The yellow region in Fig. 13 illustrates the system efficiency across these points, encompassing all discussed states and demonstrating a range from 95.5% to 97.5%. The average measured conversion efficiency of the architecture as a function of PV string 1 current shows efficiency ranging from 96.3% to 97%. These results confirm that the system efficiency always exceeds that of a single SLC. Notably, when the system is in state 4, it is possible to deactivate the SLCs, resulting in a system efficiency of 99%. Therefore, this architecture can provide higher efficiency compared to the architecture discussed in the Section I and in Table 1.

This architecture offers high efficiency, scalability, and adaptability, low-voltage component ratings, and the ability to perform string-level MPPT. However, the battery charging and discharging rates are limited, and the two-stage SLC converters increase system complexity. Therefore, future research could explore new single-stage topologies that reduce initial costs while maintaining the same functionality.

VI. CONCLUSION

This article introduced a novel PV2VB PDPP-based architecture, specifically designed for string-level MPPT while efficiently managing battery charging and discharging. In this architecture, the SLCs operate in fast loops to independently track MPPT, while a central converter, such as a boost converter, manages the battery in a slower loop. By exploring all possible operational states of the system across different battery charge/discharge rates, the architecture is shown to function effectively in modes such as SIDO-I, DISO-I, SISO-I, and SISO-II, while it is able to operate in SISO-III and SISO-IV with reconfiguration. Experimental results validate the architecture's performance and theoretical foundations, demonstrating string-level MPPT with system efficiency between 95.5% and 99%.

ACKNOWLEDGMENT

The authors extend their appreciation to Stefaan Heirman, Tim Velzeboer, and Shuang Hao for their support in the design and fabrication of the electronic safety cabinet, enabling the successful execution of our experiments. Additionally, they express their gratitude toward Prof. Dr. Pavol Bauer, Dr. Ing. Bart Roodenburg, Prof. Ir. Peter Vaessen, and Dr. Ir. Mohamad Ghaffarian Niasar for providing the necessary equipment essential for conducting our tests.

REFERENCES

[1] A. Smets, K. Jäger, O. Isabella, R. Van Swaaij, and M. Zeman, *Solar Energy: The Physics and Engineering of Photovoltaic Conversion, Technologies and Systems*. New York, NY, USA: Bloomsbury Publishing, 2016.

[2] C. S. Chin, A. Sharma, D. S. Kumar, and S. Madampath, "Singapore's sustainable Energy Story: Low-carbon energy deployment strategies and challenges," *IEEE Electrific. Mag.*, vol. 10, no. 4, pp. 84–89, Dec. 2022, doi: 10.1109/MELE.2022.3211109.

[3] A. Nazer, S. Driss, A. M. Haddadi, and S. Farhangi, "Optimal photovoltaic multi-string inverter topology selection based on reliability and cost analysis," *IEEE Trans. Sustain. Energy*, vol. 12, no. 2, pp. 1186–1195, Apr. 2021, doi: 10.1109/TSTE.2020.3038744.

[4] A. Amoorezaei, S. A. Khajehoddin, and K. Moez, "A compact cuk-based differential power processing IC with integrated magnetics and soft-switching controller for maximized cell-level power extraction," *IEEE Trans. Power Electron.*, vol. 39, no. 4, pp. 4473–4490, Apr. 2024, doi: 10.1109/TPEL.2023.3347762.

[5] D. Xu et al., "Coupling analysis of differential power processing-based PV system and its decoupling implementation of synchronous MPPT control," *IEEE Trans. Ind. Electron.*, vol. 70, no. 7, pp. 6973–6983, Jul. 2023, doi: 10.1109/TIE.2022.3201277.

[6] A. Alenezi and H. A. Hussain, "A new control approach for least processed power tracking under mismatch conditions in PV systems using differential power processing," *IEEE Trans. Ind. Appl.*, vol. 60, no. 1, pp. 532–543, Jan./Feb. 2024, doi: 10.1109/TIA.2023.3312651.

[7] P. Wang, R. C. N. Pilawa-Podgurski, P. T. Krein, and M. Chen, "Stochastic power loss analysis of differential power processing," *IEEE Trans. Power Electron.*, vol. 37, no. 1, pp. 81–99, Jan. 2022, doi: 10.1109/TPEL.2021.3099757.

[8] C. Olalla, C. Deline, D. Clement, Y. Levron, M. Rodriguez, and D. Maksimovic, "Performance of power-limited differential power processing architectures in mismatched PV systems," *IEEE Trans. Power Electron.*, vol. 30, no. 2, pp. 618–631, Feb. 2015, doi: 10.1109/TPEL.2014.2312980.

[9] P. S. Shenoy, K. A. Kim, B. B. Johnson, and P. T. Krein, "Differential power processing for increased energy production and reliability of photovoltaic systems," *IEEE Trans. Power Electron.*, vol. 28, no. 6, pp. 2968–2979, Jun. 2013, doi: 10.1109/TPEL.2012.2211082.

[10] X. Liu, X. Liu, Y. Jiang, T. Zhang, and B. Hao, "Photovoltaics and energy storage integrated flexible direct current distribution systems of buildings: Definition, technology review, and application," *CSEE J. Power Energy Syst.*, vol. 9, no. 3, pp. 829–845, 2023, doi: 10.17775/CSEEJPES.2022.04850.

[11] G. G. Farivar et al., "Grid-connected energy storage systems: State-of-the-art and emerging technologies," *Proc. IEEE*, vol. 111, no. 4, pp. 397–420, Apr. 2023, doi: 10.1109/JPROC.2022.3183289.

[12] S. S. Dobakhshari, S. H. Fathi, and J. Milimonfared, "A new soft-switched three-port DC/DC converter with high voltage gain and reduced number of semiconductors for hybrid energy applications," *IEEE Trans. Power Electron.*, vol. 35, no. 4, pp. 3590–3600, Apr. 2020, doi: 10.1109/TPEL.2019.2933182.

[13] T. Qian, Y. Yang, and W. Zhao, "A boost-type three-port resonant forward converter with flexible power flow path optimization for PV systems," *IEEE Trans. Circuits Syst. II, Exp. Briefs*, vol. 70, no. 1, pp. 161–165, Jan. 2023, doi: 10.1109/TCSII.2022.3199335.

[14] B. Zhang, P. Wang, T. Bei, X. Li, Y. Che, and G. Wang, "Novel topology and control of a non-isolated three port DC-DC converter for PV-battery power system," in *Proc. 20th Int. Conf. Elect. Mach. Syst.*, Aug. 2017, pp. 1–6, doi: 10.1109/ICEMS.2017.8056089.

[15] X. Sun, Y. Shen, W. Li, and H. Wu, "A PWM and PFM hybrid modulated three-port converter for a standalone PV/battery power system," *IEEE J. Emerg. Sel. Topics Power Electron.*, vol. 3, no. 4, pp. 984–1000, Dec. 2015, doi: 10.1109/JESTPE.2015.2424718.

[16] O. M. Akeyo, V. Rallabandi, N. Jewell, and D. M. Ionel, "The design and analysis of large solar PV farm configurations with DC-connected battery systems," *IEEE Trans. Ind. Appl.*, vol. 56, no. 3, pp. 2903–2912, May/Jun. 2020, doi: 10.1109/TIA.2020.2969102.

[17] Z. Saadatizadeh, P. C. Heris, and A. Mantooth, "High-frequency three-port DC–DC converter with zero-voltage switching operation," *IEEE Trans. Ind. Electron.*, vol. 71, no. 1, pp. 537–548, Jan. 2024, doi: 10.1109/TIE.2023.3245209.

[18] L. Senapati, A. K. Panda, M. M. Garg, and R. K. Lenka, "A systematic approach to synthesize a non-isolated TPCC with fully reconfigurable structure for RES," *IEEE Trans. Circuits Syst. II, Exp. Briefs*, vol. 69, no. 7, pp. 3314–3318, Jul. 2022, doi: 10.1109/TCSII.2022.3166976.

[19] H. Aljarajreh, D. D.-C. Lu, Y. P. Siwakoti, R. P. Aguilera, and C. K. Tse, "A method of seamless transitions between different operating modes for three-port DC-DC converters," *IEEE Access*, vol. 9, pp. 59184–59195, 2021, doi: 10.1109/ACCESS.2021.3073948.

[20] K. Li, Y. Wang, J. Lu, L. Guo, J. Wu, and H. Wang, "Research on multi-mode control strategy of high-power three-port photovoltaic DC converter," in *Proc. Int. Conf. Adv. Elect. Equip. Reliable Operation*, Oct. 2021, pp. 1–6, doi: 10.1109/AEERO52475.2021.9708322.

[21] K. Wang, W. Liu, and F. Wu, "Topology-level power decoupling three-port isolated current-fed resonant DC-DC converter," *IEEE Trans. Ind. Electron.*, vol. 69, no. 5, pp. 4859–4868, May 2022, doi: 10.1109/TIE.2021.3082066.

[22] H. Hasabelrasul, Z. Cai, L. Sun, X. Suo, and I. Matraji, "Two-stage converter standalone PV-battery system based on VSG control," *IEEE Access*, vol. 10, pp. 39825–39832, 2022, doi: 10.1109/ACCESS.2022.3165664.

[23] K. R and R. Kalpana, "An isolated dual-input half-bridge DC–DC boost converter with reduced circulating power between input ports," *IEEE Can. J. Elect. Comput. Eng.*, vol. 45, no. 1, pp. 68–76, Jan. 2022, doi: 10.1109/ICJECE.2021.3130723.

[24] A. Nazer, O. Isabella, and P. Manganiello, "PV to virtual bus parallel differential power processing architecture for photovoltaic systems," *IEEE Trans. Ind. Electron.*, vol. 72, no. 5, pp. 4833–4843, May 2025, doi: 10.1109/TIE.2024.3468645.

[25] A. Nazer, O. Isabella, and P. Manganiello, "Dynamic analysis of photovoltaic to virtual bus parallel differential power processing architecture," *IEEE Trans. Ind. Electron.*, vol. 72, no. 8, pp. 8082–8093, Aug. 2025, doi: 10.1109/TIE.2025.3528473.

[26] A. Nazer, O. Isabella, and P. Manganiello, "A comprehensive classification of state-of-the-art distributed maximum power point tracking architectures for photovoltaic systems," *IEEE Open J. Ind. Electron. Soc.*, vol. 6, pp. 738–763, 2025, doi: 10.1109/OJIES.2025.3565902.

[27] A. Nazer, P. Manganiello, and O. Isabella, "A virtual bus parallel differential power processing configuration for photovoltaic applications," *Math. Comput. Simul.*, vol. 224, pp. 49–62, 2024, doi: 10.1016/j.matcom.2023.06.001.

[28] K. Liu, K. Li, Q. Peng, and C. Zhang, "A brief review on key technologies in the battery management system of electric vehicles," *Front. Mech. Eng.*, vol. 14, no. 1, pp. 47–64, Mar. 2019, doi: 10.1007/s11465-018-0516-8.

[29] K. K. Duru, C. Karra, P. Venkatachalam, S. A. Betha, A. A. Madhavan, and S. Kalluri, "Critical insights into fast charging techniques for lithium-ion batteries in electric vehicles," *IEEE Trans. Device Mater. Rel.*, vol. 21, no. 1, pp. 137–152, Mar. 2021, doi: 10.1109/TDMR.2021.3051840.

[30] B. Zhao, Q. Song, W. Liu, and Y. Sun, "Overview of dual-active-bridge isolated bidirectional DC–DC converter for high-frequency-link power-conversion system," *IEEE Trans. Power Electron.*, vol. 29, no. 8, pp. 4091–4106, Aug. 2014, doi: 10.1109/TPEL.2013.2289913.

[31] S. S. Williamson, A. K. Rathore, and F. Musavi, "Industrial electronics for electric transportation: Current state-of-the-art and future challenges," *IEEE Trans. Ind. Electron.*, vol. 62, no. 5, pp. 3021–3032, May 2015, doi: 10.1109/TIE.2015.2409052.